

1 **Global trends in air-water CO₂ exchange over seagrass meadows revealed by**
 2 **atmospheric Eddy Covariance**

3 **¹Bryce Van Dam, ²Pierre Polsemaere, ³Aylin Barreras-Apodaca, ⁴Christian Lopes, ³Zulia**
 4 **Sanchez-Mejia, ^{5,6}Tatsuki Tokoro, ⁶Tomohiro Kuwae, ⁷Lucia Gutiérrez Loza, ⁷Anna**
 5 **Rutgersson**

6
 7 ¹ Institute of Coastal Research, Helmholtz-Zentrum Geesthacht (HZG), Geesthacht, 21502,
 8 Germany

9 ² IFREMER, Laboratoire Environnement et Ressources des Pertuis Charentais (LER-PC),
 10 BP133, 17390, La'Tremblade, France.

11 ³ Instituto Tecnológico de Sonora, Ciudad Obregón, Sonora, México

12 ⁴ Dept. of Biology and The Institute of Environment, Florida International University, 11200 SW
 13 8th Street, Miami, FL 33199, USA

14 ⁵ Coastal and Estuarine Environment Research Group, Port and Airport Research Institute,
 15 Yokosuka, Japan

16 ⁶ National Institute for Environmental Studies, Center for Global Environmental Research
 17 (CGER), Office for Atmospheric and Oceanic Monitoring, Onogawa, Tsukuba, Ibaraki, Japan

18 ⁷ Department of Earth Sciences, Uppsala University, Uppsala, Sweden

19

20 Corresponding author: Bryce Van Dam, (Bryce.Dam@hzg.de)

21

22 **Key Points:**

- 23 • Direct measurements show that air-water CO₂ exchange over seagrass meadows is of
 24 similar magnitude to carbon burial rates
- 25 • Key drivers are tidal forcing, temperature, light, and wind, which trade off in importance
 26 over hourly-seasonal time scales
- 27 • Surface drag coefficients were greater than open water prediction, suggesting a near-
 28 universal gas transfer enhancement across all sites
- 29

30 Abstract

31 Coastal vegetated habitats like seagrass meadows can mitigate anthropogenic carbon emissions
32 by sequestering CO₂ as “blue carbon” (BC). Already, some coastal ecosystems are actively
33 managed to enhance BC storage, with associated BC stocks included in national greenhouse gas
34 inventories or traded on international markets. However, the extent to which BC burial fluxes are
35 enhanced or counteracted by other carbon fluxes, especially air-water CO₂ flux (FCO₂) remains
36 poorly understood. To this end, we synthesized all available direct FCO₂ measurements over
37 seagrass meadows made using a common method (atmospheric Eddy Covariance), across a
38 globally-representative range of ecotypes. Of the four sites with seasonal data coverage, two
39 were net CO₂ sources, with average FCO₂ equivalent to 44 - 115% of the global average BC
40 burial rate. At the remaining sites, net CO₂ uptake was 101 - 888% of average BC burial. A
41 wavelet coherence analysis demonstrates that FCO₂ was most strongly related to physical factors
42 like temperature, wind, and tides. In particular, tidal forcing appears to shape global-scale
43 patterns in FCO₂, likely due to a complex suite of drivers including: lateral carbon exchange,
44 bottom-driven turbulence, and pore-water pumping. Lastly, sea-surface drag coefficients were
45 always greater than prediction for the open ocean, supporting a universal enhancement of gas-
46 transfer in shallow coastal waters. Our study points to the need for a more comprehensive
47 approach to BC assessments, considering not only organic carbon storage, but also air-water CO₂
48 exchange, and its complex biogeochemical and physical drivers.

49 Plain Language Summary

50 Carbon storage is a valuable ecosystem service of seagrass meadows, serving as a possible
51 pathway to draw down atmospheric carbon dioxide (CO₂) levels. However, this approach may be
52 unsuccessful if carbon storage in sediments is exceeded by the release of CO₂ from the water. To
53 better understand the scope of this problem, we compiled all available measurements of air-water
54 CO₂ exchange over seagrass meadows. We found that rates of CO₂ release or uptake were indeed
55 large, even when compared with potential rates of carbon storage in seagrass soils. However,
56 these large air-water exchanges of CO₂ did not occur for the same reason everywhere. While
57 light availability was sometimes a strong predictor of air-water CO₂ exchange, tidal mixing and
58 temperature were also very important, revealing a much more complex network of drivers than
59 previously thought. Despite these diverse conditions, we found one key similarity across all sites,
60 in that rates of air-water gas transfer appear to always be greater than would be expected for the
61 open ocean. Taken together, the results of our study show that assessments of carbon storage in
62 coastal seagrass ecosystems will be incomplete if they do not consider exchanges of CO₂
63 between the water and air.

64 1. Introduction

65 The coastal ocean plays a disproportionately large role in global and regional carbon (C) cycles
66 (Fennel et al., 2019; Friedlingstein et al., 2019; Laruelle et al., 2018). In particular, seagrass-
67 inhabited regions receive large quantities of terrestrial and marine organic carbon, much of
68 which is sequestered in sediments and stabilized by extensive root mats (Prentice et al., 2020;
69 Röhr et al., 2018). Carbon fixed locally by seagrasses and their epiphytes is also buried here,
70 constituting a net removal of C from the atmosphere (Duarte et al., 2005; Kennedy et al., 2010).
71 Despite some uncertainty regarding its ultimate source, this ‘blue carbon’ reservoir (Macreadie et
72 al., 2019; Kuwae and Hori 2019) is a globally significant, yet sensitive, carbon stock
73 (Fourqurean et al., 2012). However, these relatively high C burial rates in seagrass meadows -
74 reaching $0.22 \text{ g C m}^{-2} \text{ yr}^{-1}$ (Duarte et al., 2005) - must also be considered in the context of other
75 C flows through the ecosystem, which act synergistically or antagonistically to increase or
76 decrease net C sequestration.

77 For example, the biotic or abiotic formation and burial of calcium carbonate in seagrass beds
78 consumes alkalinity, thereby generating CO_2 (Burdige and Zimmerman 2002; Burdige et al.,
79 2010; Hu and Burdige 2007). Likewise, the degradation of organic matter in anoxic sediments
80 produces CH_4 and N_2O at rates that may affect the net global warming potential of seagrass
81 meadows (Oreska et al., 2020). As a result, some seagrass beds, especially those receiving large
82 loads of allochthonous organic matter (Al-Haj and Fulweiler 2020), or those where calcification
83 rates are high (Howard et al., 2018), can be pushed towards net C source status, despite high
84 rates of autotrophic C fixation (Macreadie et al., 2017). The extent to which calcification
85 mitigates photosynthetic CO_2 uptake, pushing seagrass ecosystems towards CO_2 source status
86 remains a hotly debated topic (Howard et al., 2018; Sanders et al., 2019). While it is suggested
87 that CO_2 uptake is not affected by carbonate precipitation because carbonate minerals are largely
88 imported from adjacent systems (Saderne et al., 2019), confirmation by direct CO_2 flux
89 measurements does not yet exist.

90 Seagrass meadows may also vary between net ecosystem heterotrophy and autotrophy over daily
91 to weekly time scales (Berg et al., 2019; Gazeau et al., 2005; Van Dam et al., 2019a). Elsewhere,
92 the anaerobic generation of alkalinity, largely through sulfate reduction and burial (Dollar et al.,
93 1991) and denitrification (Eyre and Ferguson 2002), can increase the buffering capacity of
94 overlying water, enhancing atmospheric CO_2 uptake. Advection can also play a role, as
95 seagrasses in river-dominated estuaries may receive waters over-saturated in CO_2 , which is
96 subsequently degassed in the wind-exposed coastal zone (Röhr et al., 2018). Regardless of the
97 mechanism, it is clear that C sequestration in ‘blue carbon’ ecosystems is not simply the product
98 of long-term organic carbon burial in sediments. Many other processes consume or produce
99 dissolved inorganic carbon (DIC), such as calcification and anaerobic metabolism, thereby
100 affecting air-water CO_2 fluxes (FCO_2), pushing these ecosystems towards net carbon sink or net
101 source, independent of the organic carbon burial flux.

102 Given the broad global distribution of seagrasses, and the various coastal typologies they inhabit,
103 it is no surprise that net ecosystem metabolism exhibits substantial geographic trends (Duarte et
104 al., 2010). Likewise, FCO_2 in these systems is not uniform. In some regions, for example, light

105 limitation of photosynthesis may play a critical role in net ecosystem productivity (Berg et al.,
106 2019; Long et al., 2015) and CO₂ uptake (Gazeau et al., 2005; Tokoro et al., 2014). Elsewhere,
107 due to greater turbidity or water depth, this factor may carry little leverage, exceeded in
108 importance by tides (Polsenaere et al., 2012) or water temperature (Van Dam et al., in review).
109 Where temperature and biology allow, net ecosystem calcification may instead dominate water
110 column carbonate chemistry (Perez et al., 2018; Van Dam et al., 2019a). These reasons and
111 others may contribute to differences in FCO₂ for seagrass meadows located at comparable
112 latitudes or in similar climates.

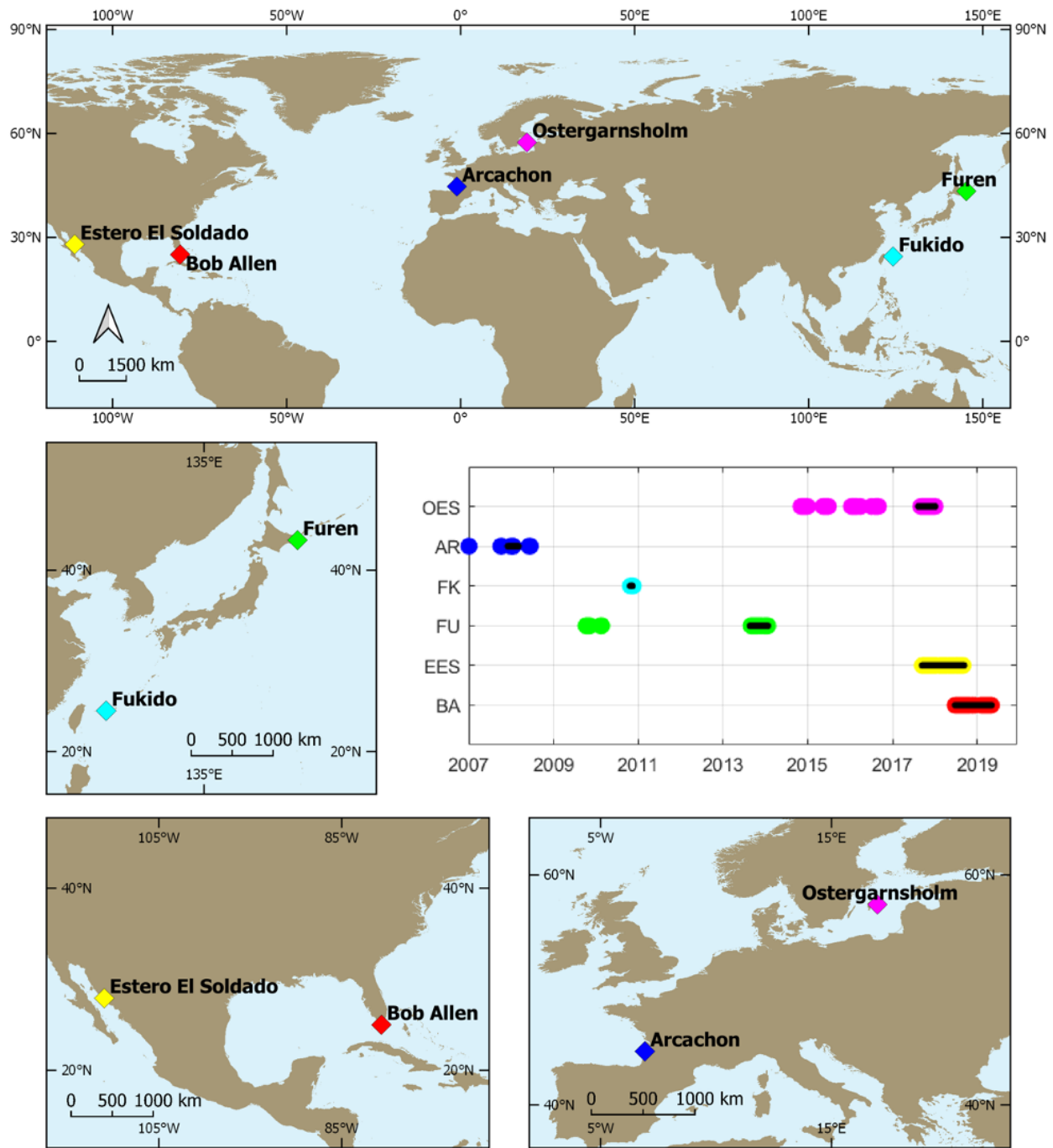
113 Rates of carbon burial can be reliably assessed using natural and anthropogenic radioactive
114 tracers, integrating this process over a sufficiently long period as to accurately characterize burial
115 over decadal to centurial scales. This is in stark contrast to FCO₂, where extreme temporal
116 variability complicates attempts to integrate this flux over time. Existing ‘bulk transfer’
117 approaches to quantifying FCO₂ rely on discrete measurements of CO₂ partial pressure ($p\text{CO}_2$),
118 which often miss out on high-frequency variability. These $p\text{CO}_2$ measurements are then
119 combined with a gas transfer coefficient, the parameterization of which is notoriously
120 challenging due to the diverse physical forcing of air-water gas exchange in shallow coastal
121 waters (Borges et al., 2004). For these reasons, direct measurements of FCO₂ are desirable,
122 relative to parameterized estimates. Atmospheric eddy-covariance (EC) has been used for
123 decades to measure turbulent exchanges of gas and energy over terrestrial ecosystems (Aubinet
124 et al., 2000; Baldocchi 2003), and the open ocean (Butterworth and Miller, 2016; Garbe et al.,
125 2014; Wanninkhof et al., 2009). However, only recently has this approach begun to be used at
126 nearshore intertidal or subtidal habitats (Chien et al., 2018; Honkanen et al., 2018; Ikawa et al.,
127 2015; Rey-sánchez et al., 2017) including seagrass meadows (Polsenaere et al., 2012; Tokoro et
128 al., 2014; Van Dam et al., in rev). Advantages of direct EC measurements of FCO₂ include: 1)
129 continuous temporal coverage, 2) existence of standard methods for data processing, and 3) non-
130 invasive and spatially representative measurements.

131 While direct FCO₂ measurements over seagrass meadows have existed for roughly a decade
132 (Polsenaere et al., 2012), and some regional synthetic efforts have been made (Tokoro et al.,
133 2014), these individual datasets have yet to be synthesized globally. Therefore, a set of very
134 basic questions remains unanswered. Are there global patterns explaining why some seagrass
135 meadows are CO₂ sinks and others are sources? Are these reasons typological, climatological, or
136 simply latitudinal in nature? Are there any generalizable features of air-water CO₂ exchange
137 across these diverse coastal habitats? These questions are central to ‘blue carbon’ science (Legge
138 et al., 2020; Macreadie et al., 2019), but have yet to be addressed. In the present study, we
139 synthesize a dataset of direct EC measurements of air-sea FCO₂ over seagrasses. While this
140 dataset is limited to only sites in the Northern hemisphere, it is the most complete synthesis to
141 date, representing a broad range in latitude and ecosystem characteristics. We describe global
142 trends in FCO₂, discuss temporal and spatial variability and associated controls, and compare
143 FCO₂ with literature estimates of carbon burial. A spectral decomposition is also used to identify
144 sets of physical drivers important across temporal scales.

145 **2. Materials and Methods**

146 **2.1. Study Sites**

147 Direct EC measurements of FCO₂ were acquired for six subtidal or intertidal sites with seagrass
 148 coverage. Together, these sites represent a broad zonal (110° W to 145° E) and latitudinal (24° N
 149 to 57° N) range (Figure 1), and are described in table 1, along with the nearest recorded coastal
 150 typology from Dürr et al. (2011).



152 **Figure 1.** Site Maps, including inset figure of data coverage for each site, where the black bars
 153 indicate the subset of reasonably ‘continuous’ data used for the wavelet coherence analysis.

Site Name		Coastal Typology	Seagrass Community	Mean Daily Tidal Range (Tidal category)	Seagrass Biomass (gC or gDW m ⁻²)	Lat-Long (decimal degree)	Days of data available (# Measurement Periods)	Methods Reference
Bob Allen Keys, USA	BA	Type VI (Karst)	<i>Thalassia testudinum</i>	0.048 m (small-tidal)	4.8 gC m ⁻²	25.03 -80.68	314 (1)	Van Dam et al. (2020)
Estero El Soldado, Mexico	EES	Type VII (Arheic)	<i>Zostera marina</i>	0.40 m (large-tidal•)	-	27.95 -110.97	357 (1)	Benítez-Valenzuela& Sanchez-Mejia 2020)
Furen lagoon, Japan	FU	Type I (Small Deltas)	<i>Zostera marina</i>	0.87 m (large-tidal)	16-318 g DW m ⁻²	43.33 145.26	146 (3)	Tokoro et al. (2014)
Fukido estuary, Japan	FK	Type I (Small Deltas)	<i>Cymodocea serrulata</i> , <i>Thalassia Hemprichii</i> , <i>Enhalus acoroides</i>	0.93 m (large-tidal)	32-88 g DW m ⁻²	24.49 124.23	25 (1)	Tokoro et al. (2014)
Arcachon Bay, France	AR	Type II (Tidal Systems)	<i>Zostera spp.</i>	1.8 m (large-tidal)	93.4 - 114.9 g DW m ⁻²	44.67 -1.67	530 (2)	Polsenaere et al. (2012)
Östergarnsholm, Sweden	OES	Type IV (Fjords or Fjaerds)	Unknown	<0.5 (small -tidal)	-	57.45 18.98	1,156 (1)	Lucía Gutiérrez-Loza et al. (2019)

154 **Table 1.** Summary table describing each site considered in this study, including the coastal
 155 typology (Dürr et al., 2011), and seagrass community and coverage statistics. Community and
 156 cover statistics are from Plus et al. (2010) and Carmen et al. (2019) for AR, from Tokoro et al.
 157 (2014) For FU and FK, from Armitage & Fourqurean (2011) for BA. Tidal ranges shown here
 158 were calculated from mean daily statistics over the entire study period, except for OES, where
 159 we apply a literature value of 0.5m (Sahlée et al., 2008). EES is considered a “large-tidal” site
 160 because it is located inside a tidal inlet where appreciable tidal currents exist despite a relatively
 161 low tidal range.

162 **2.2. EC Measurements**

163 While different analytical instruments were used at each site (Table 1), all EC measurements
 164 were conducted using coincident and rapid (10-20 Hz) measurements of CO₂ concentration and
 165 3-D wind velocity. All EC systems relied on infrared gas analyzers (IRGA) produced by LI-COR
 166 Biosciences, USA. These IRGAs were either of an open- or closed-path configuration,
 167 depending on the environmental and power conditions at each site. Further information regarding
 168 the specific EC configurations used at each site can be found in the references shown in Table 1.

169 **2.3. Data QA/QC**

170 For all datasets processed using EddyPro software (Licor Biosciences, USA), data were screened
171 to remove records with QC code (Burba 2010) greater than 1, resulting in a removal of 11.6% of
172 the full dataset. Next, in an effort to screen out data where a terrestrial influence was likely, we
173 removed results where the shear conditions indicated a non-marine flux footprint. As described
174 later, we discarded FCO₂ results when the ratio of u^*/U_{mean} exceeded a threshold of 0.139, which
175 was set as 150% of the average u^*/U_z (0.0924). This step resulted in the removal of an additional
176 14.6% of the data following QC code screening. Lastly, FCO₂ values greater than 3 standard
177 deviations from the mean ($\text{FCO}_2 > 10.4 \mu\text{mol m}^{-2} \text{s}^{-1}$) were considered anomalous and were
178 removed, representing a final 1.3% of the remaining dataset. Cumulatively, these screening steps
179 removed 25.5% of the initial, post-processed dataset. In keeping with convention, negative FCO₂
180 indicates a net CO₂ uptake, while positive values represent CO₂ emission.

181 **2.4. Energy balance**

182 Energy balance assessments are important components of terrestrial EC studies, as these energy
183 flows (radiative as well as latent and sensible heat exchanges) directly control local water
184 budgets and hence many ecosystem processes. In an idealized system, inputs of energy net solar
185 radiation (R_n) are exactly balanced by latent (i.e. evaporative) and sensible heat fluxes, LE and H
186 respectively. Any departure from the 1:1 relationship between R_n and total heat loss (H+LE),
187 suggests that EC measurements are missing some energy flux. This could be due to non-
188 stationary conditions, when spatial gradients in a variable (i.e. temperature) are advected past the
189 measurement site, causing, for example, LE+H to be greater/less than R_n . While these
190 measurements may well be ‘real’, they can also be problematic because they indicate that factors
191 outside the flux footprint have influenced the measured vertical fluxes at a given time. Likewise,
192 energy can be stored in (or lost from) standing water when its temperature changes. In the
193 present study, we have quantified this energy flux (J) and considered it in subsequent budget
194 assessments. Because of the very high heat capacity of water, frequent departures from the 1:1
195 relationship between H+LE+J and R_n can be taken as indicators of lateral water exchange. This
196 is of course concerning for EC studies of FCO₂ in shallow waters, where our goal is to attribute
197 measured FCO₂ to processes happening inside the flux footprint (i.e. the seagrass meadow).

198 At sites where measurements of water temperature, water height, net solar radiation (R_n ; W m^{-2}),
199 latent heat flux (LE; W m^{-2}), and sensible heat flux (H; W m^{-2}) were available, it was possible to
200 construct an approximate energy budget. We determine the closure of this energy balance as the
201 difference between R_n and the sum of LE, H, and J, integrated over 24 hours (BA, EES, FK,
202 OES) or 6 hours when water-side measurements were limited (AR). When R_n data were absent,
203 R_n was estimated from photosynthetically active radiation (PAR; $\mu\text{mol photons m}^{-2} \text{s}^{-1}$) using an
204 empirical relationship ($R_n = -0.60 * \text{PAR} - 0.12$; linear $R^2 = 0.98$) constructed using the
205 combined dataset from this study.

206 The energy balance at OES is somewhat more challenging to assess, in part because of a
207 relatively complex bathymetry, which makes it difficult to estimate the water depth over which
208 the water-column energy storage (J) should be integrated. The presence of seasonal and periodic
209 stratification, as well as greater absolute water depths (up to 40 m) further complicate the energy

210 balance here (Rutgersson et al., 2020). Therefore, for OES, we calculated J using a water depth
211 of 5 m, which was the depth at which water temperature was measured.

212 **2.5. Time-Frequency Analysis**

213 A wavelet coherence analysis (Grinsted et al., 2004; Torrence and Compo 1998) was carried out
214 to analyze the dependence of FCO₂ on net solar radiation (R_n), water depth (Z_{water}), air
215 temperature (T_{air}), water temperature (T_{water}), wind speed (U_{mean}), and wind direction (U_{dir}). Due
216 to the sporadic nature of these coastal EC deployments, the temporal coverage is somewhat
217 patchy, creating a problem for time-series analysis. So, prior to wavelet coherence analysis, the
218 largest period of contiguous data availability was identified for each site (black bars shown in
219 Figure 1), and only this period was used for subsequent wavelet analysis. This necessary choice
220 results in an improved data quality at hourly to monthly time scales, but necessarily involves a
221 loss of information at longer scales. Gaps in the pseudo-continuous datasets for each site were
222 filled with mean statistics for each variable, and the edges were padded with zeros. We forced
223 each dataset into a normal distribution, applied a Morlet wavelet to the time series (Grinsted et
224 al., 2004), and estimated the 95% confidence intervals with 15 Monte Carlo simulations.

225 **3. Results and Discussion**

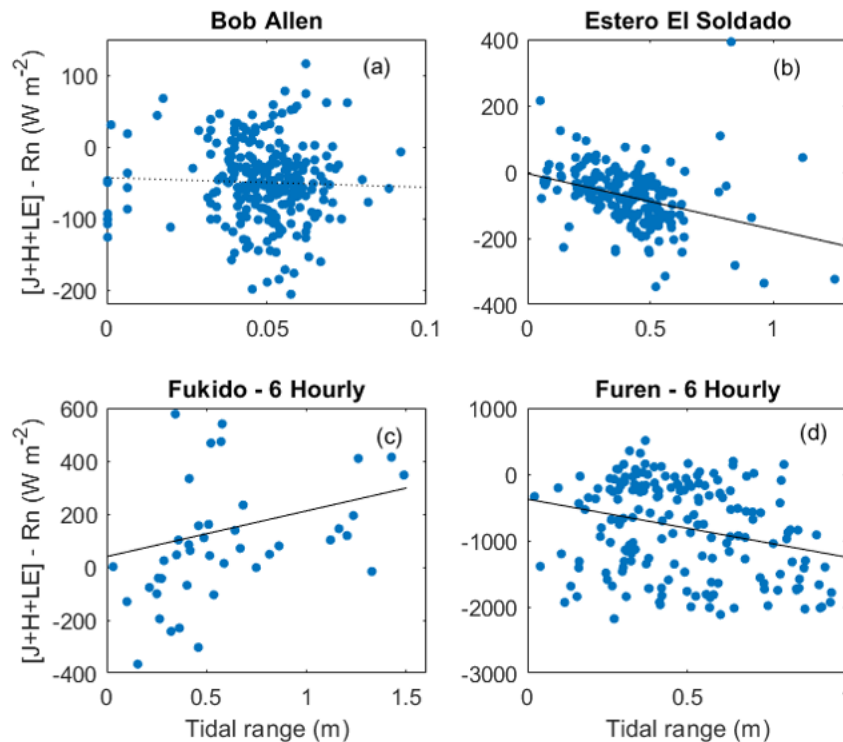
226 **3.1. Energy balance**

227 The energy balance closure was best for BA, with daily average R_n closely balanced by net heat
228 losses ($H+LE+J$) (Figures 2a, S1). This was not the case for the remaining sites for which a
229 complete energy balance could be assessed (EES, FK, FU, AR, OES). At EES, most daily
230 average heat losses ($H+LE+J$) fell below the 1:1 line (Figures 2b, S1), indicating either a
231 measurement error, or the presence of a missing heat flux that we currently do not account for.
232 At EES, this missing heat flux is plausibly related to horizontal advection and tidal exchange
233 with the adjacent upwelling system. Similarly, low heat losses relative to R_n were observed at
234 OES (Figure 3b), but the microtidal nature of this site suggests that the energy budget imbalance
235 here could be related to horizontal advection and wind driven upwelling. The energy balance is
236 further complicated at OES due to periodic stratification and variable water depths, and our
237 approach of assuming a single, average water height to calculate J, may not be appropriate.

238 At FU, $H+LE+J$ was always much less than R_n , indicating that water column heating was a
239 major, yet unaccounted for, energy sink. In contrast to the previous sites where $H+LE+J$ was
240 typically less than R_n (EES, OES, FU), daily heat losses were always greater than R_n at both AR
241 and FK (Figures 2c, 3a, S1). This suggests the presence of an additional heat source, beyond net
242 solar radiation (R_n). Since tidal ranges are relatively large at both AR and FK, we suggest that
243 tidal mixing was the source of warmer water, allowing heat losses through H and LE to exceed
244 net solar inputs.

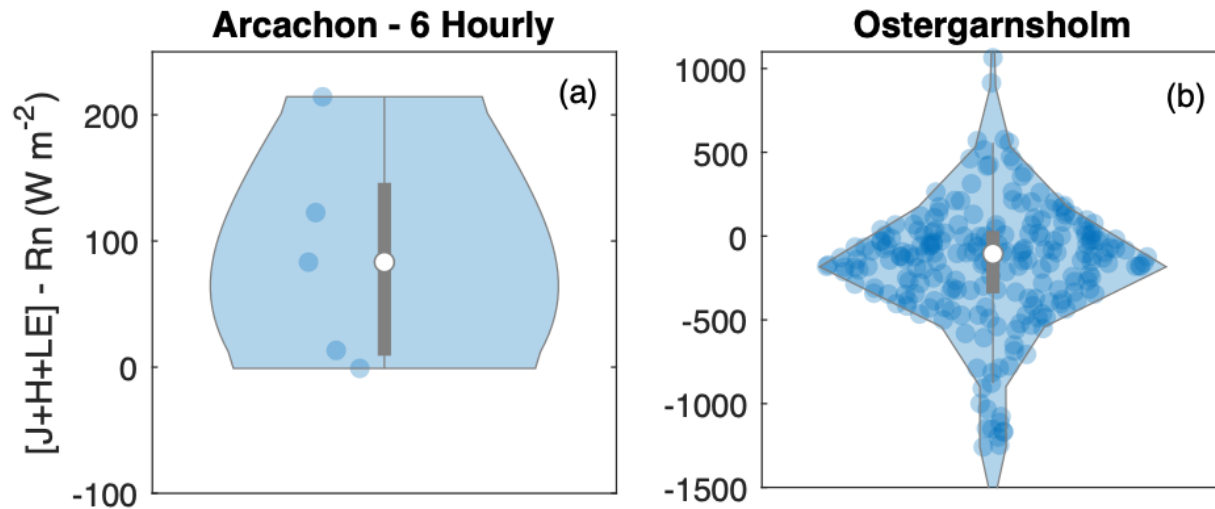
245 To further illustrate the role of tidal forcing on energy budgets, we calculate an energy balance
246 residual (EBR) as ($EBR=[J+H+LE] - R_n$), which represents the departure from the 1:1 line in
247 Figure S1. When EBR is plotted against the range in water height, it becomes clear that tidal
248 forcing plays a key role in governing energy balances across a global distribution of seagrass

249 meadows (Figures 2 and 3). At both microtidal (BA) and tidal (EES and FK) sites, the intercept
 250 of EBR with tidal range is not significantly different from zero ($\alpha = 0.05$), indicating that the
 251 energy budget is in approximate closure when tidal forcing is not present. The y-intercept was
 252 not zero at FU ($-374.7 \pm 243.9 \text{ W m}^{-2}$), but the presence of a significant negative relationship
 253 between EBR and tidal range supports the role of tidal exchange as a sink for heat.



254
 255 **Figure 2.** Energy balance residual EBR (difference between $J+H+LE$ and R_n) versus tidal range
 256 for BA (a), EES (b), FK (c), and FU (d). Linear slopes for EES, FK, and FU are significantly
 257 different from zero and are shown in bold, while the slope is insignificant for BA (a).

258 At BA, there appears to be little energy ‘leakage’ due to tidal advection, as EBR does not vary
 259 with the daily range in water height (Figure 2a). However, at both tidal sites (EES and FK), there
 260 is a significant linear correlation between EBR and the tidal range ($\alpha = 0.05$). This relationship is
 261 positive for FK, such that energy inputs from R_n are exceeded by loss through LE, H, or J, with
 262 the difference increasing with tidal range (Figure 2c). This positive EBR implies an input of
 263 relatively warm water to the FK embayment, a likely event for a subtropical site during the
 264 summer (data for FK are from 23 July to 17 August 2011). The trend is reversed at EES, with
 265 EBR becoming more negative with increasing daily tidal range, implying a ‘leakage’ of energy
 266 via tidal exchange (Figure 2b). Because the seagrass meadows at EES are influenced by seasonal
 267 upwelling in the eastern Gulf of California (Lluch-Cota 2000), such a heat exchange between
 268 warm coastal waters and cooler, recently upwelled water appears plausible.



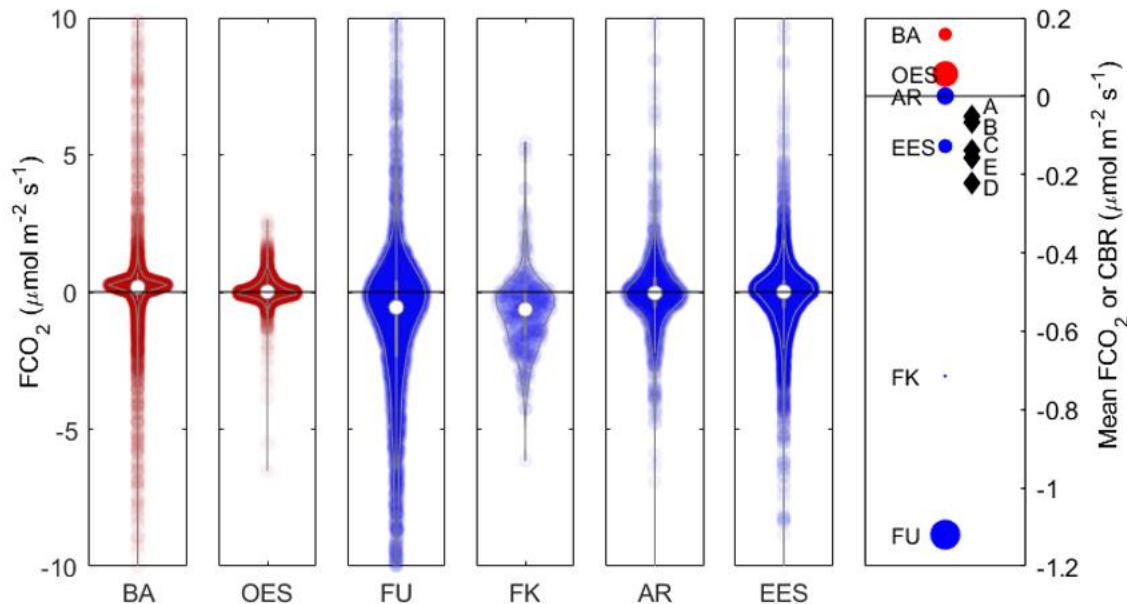
269

270 **Figure 3.** Violin plots of EBR for AR (a) and OES (b).

271 We used direct, EC measurements of heat fluxes as a conservative tracer, and showed that tidal
 272 forcing can explain large-scale trends in energy balances, despite some key site-specific
 273 differences. Because the subset of three sites considered here (BA, EES, FK) are at
 274 approximately the same latitude (Table 1), the impact of latitudinal differences in LE (Figure 6)
 275 can be excluded as a secondary factor. In subsequent sections, we will extend the results of this
 276 analysis to a non-conservative constituent, CO₂. We will discuss the impact of tidal mixing on
 277 air-water CO₂ exchange, in the context of the coastal ‘blue carbon’ sink.

278 **3.2. General patterns and trends in FCO₂**

279 FCO₂ was highly variable at all sites, fluctuating between sink (negative FCO₂) and source
 280 (positive) over the study period. Averaged over the entire study period, however, FCO₂ was
 281 negative for four sites (EES, FU, FK, AR) and positive for the other two sites (BA, OES). The
 282 spread of FCO₂ in micro-tidal regions (OES, BA) was much more narrow range than in tidal
 283 areas (FU, FK, AR, EES), suggesting that the general relationship between tidal forcing and
 284 energy fluxes (Figure 2) also applies to air-water CO₂ exchange.



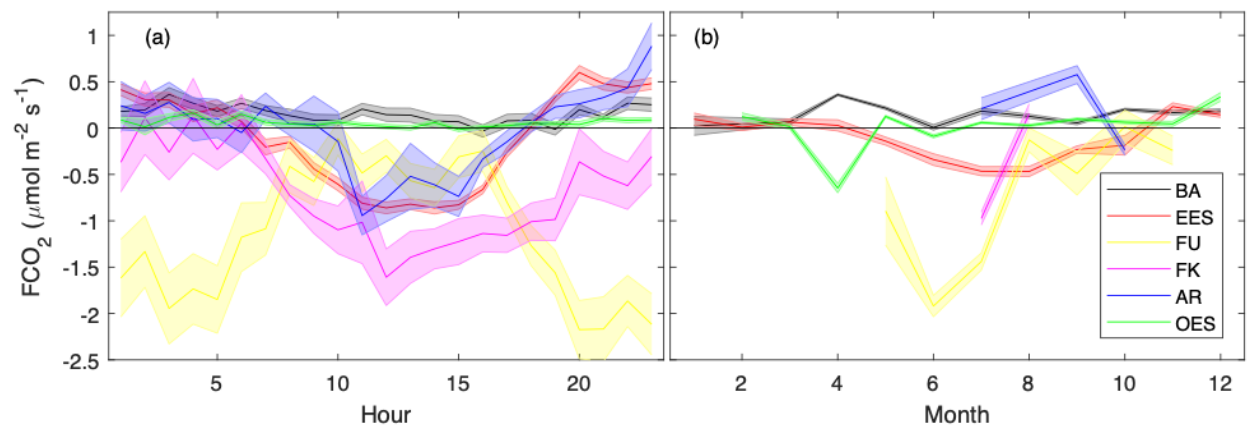
285
 286 **Figure 4.** Violin plots of FCO_2 for large-tidal (blue) and small-tidal (red) sites. In the right plot,
 287 literature values of carbon burial rates (CBR; black diamonds) are shown alongside average
 288 FCO_2 values (blue and red circles), on the same y-axis. The circles are scaled by the number of
 289 measurements available for each site. CBR averages are from Samper-Villarreal et al., 2018 (A),
 290 Prentice et al., 2020 (B), Duarte et al., 2005 (C), Kennedy et al., 2010 (D), and Sanders et al.,
 291 2019 (E).

292 These average CO_2 evasion/invasion rates are plotted (Figure 4b) alongside organic carbon burial
 293 rates (CBR) taken from a global literature review (Samper-Villarreal et al., 2018 [A], Prentice et
 294 al., 2020 [B], Duarte et al., 2005 [C], Kennedy et al., 2010 [D], and Sanders et al., 2019 [E]).
 295 Converted into the same unit as FCO_2 , these literature CBRs ranged from -0.025 to $-0.23 \mu\text{mol C}$
 296 $\text{m}^{-2} \text{s}^{-1}$, for a global average of $-0.13 \pm 0.082 \mu\text{mol C m}^{-2} \text{s}^{-1}$. The comparison of CBR with FCO_2
 297 should be made with some caution, as CBR represents time scales much longer (decades to
 298 centuries) compared with our FCO_2 measurements, for which the longest available dataset is just
 299 over three years long.

300 Nevertheless, for the sites with complete seasonal coverage (BA, EES, FU, OES), it is apt to
 301 make a comparison between the rate of carbon storage in sediments and the exchange of CO_2
 302 with the atmosphere. As is evident in Figure 4b, FCO_2 is of similar magnitude to CBR (not
 303 always the same direction), indicating that both of these biogeochemical fluxes are relevant to
 304 the carbon budget of seagrass meadows. Considering an average CBR of $0.126 \mu\text{mol m}^{-2} \text{s}^{-1}$, net
 305 emissions at BA released CO_2 to the atmosphere at a rate comparable to 125% of mean global
 306 organic carbon burial ($100\% * 0.158/0.126 = 125\%$). Assuming lateral import and export of DIC
 307 and TA were balanced, which is plausible at this site (Van Dam et al., in press), the net effect of
 308 this CO_2 emission was to transition the site from a sink for carbon into a small source. It is likely
 309 that the relatively high calcification rates in Florida Bay (Howard et al., 2018) are responsible for
 310 generating CO_2 in excess of photosynthetic uptake, pushing this site towards net CO_2 emissions.
 311 This is a noteworthy finding in light of the commonly-held view that carbonate-rich seagrass

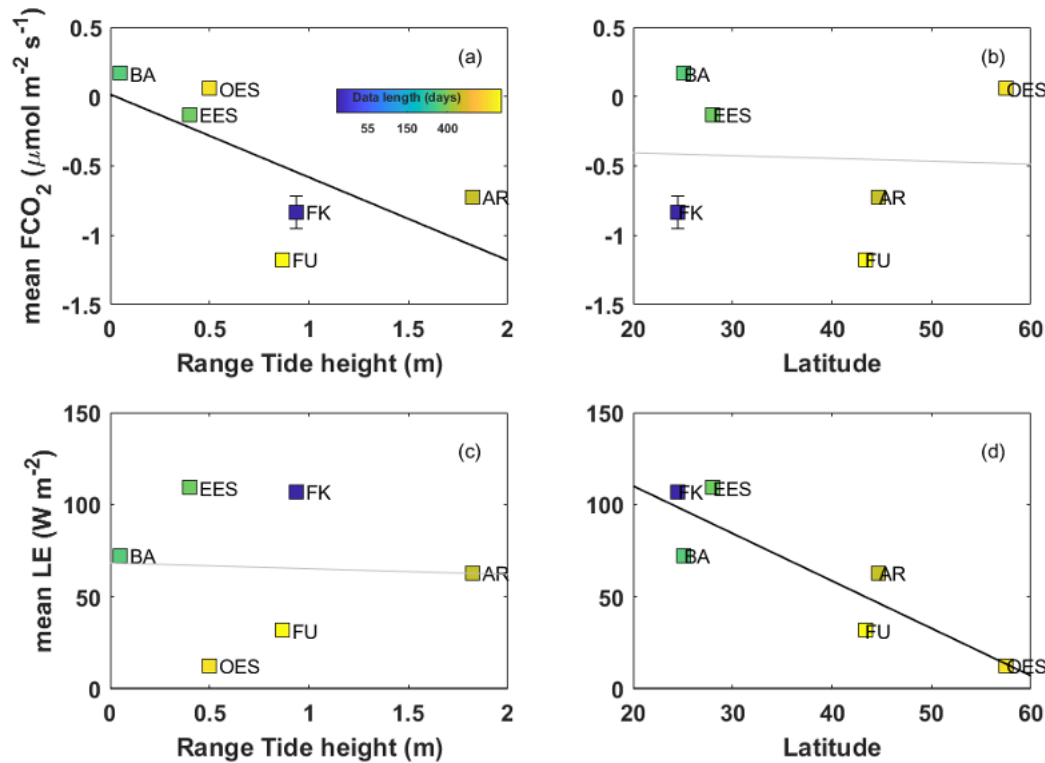
312 meadows can still be CO₂ sinks due to the import of allochthonous CaCO₃ (Saderne et al., 2019).
 313 Our finding of net CO₂ emission at BA is the first direct indication that calcification in seagrass
 314 meadows can be sufficient to offset autotrophic CO₂ uptake.

315 Likewise, net CO₂ emissions at OES were 44% of average global CBR. It should be noted that
 316 the greater water depth with some wind directions at OES means that water-column processes
 317 are likely more important here than at the other sites. At the remaining sites, net negative FCO₂
 318 uptake increased carbon uptake by 888% (FU) and 101% (EES), relative to global average CBR.
 319 As discussed later, net CO₂ uptake at these “large-tidal” sites does not necessarily point to
 320 increased carbon storage, but rather export of DIC or import of TA to/from adjacent waters. This
 321 simple assessment indicates that the consideration of only CBR or FCO₂ alone will bias the
 322 magnitude, or even sign (in the case of BA) of the coastal carbon sink. Therefore, we point to a
 323 clear need for site-specific measurements of both annually-integrated FCO₂ (by EC, for example)
 324 and CBR, which together may significantly increase the reliability of coastal carbon accounting.



325 **Figure 5.** Daily (a) and seasonal (b) climatology of mean FCO₂ for all sites. Negative values of
 326 FCO₂ indicate a net CO₂ uptake, while positive values show emission. The shaded areas
 327 represent the SE of mean FCO₂ at each hour.
 328

329 Differences were also evident in the temporal trends in FCO₂ (Figure 5). Some sites exhibited a
 330 clear diel cycle of CO₂ uptake (EES, FK, AR) or release (FU) during the day, while other sites
 331 were relatively consistent CO₂ sources (BA, OES). A significant global trend of decreasing latent
 332 heat flux (LE) with increasing latitude is evident (Figure 6d), which is expected given the similar
 333 global trend of decreasing insolation at higher latitude. On the contrary, no relationship was
 334 observed between FCO₂ and latitude (Figure 6b). Instead, as suggested by the variation in FCO₂
 335 with tidal setting (Figure 4), and the poor energy balance closure for large-tidal sites (Figure 2),
 336 the best predictor for site-averaged FCO₂ was in fact tidal range (Figure 6a).



337
 338 **Figure 6.** Scatter plots of mean FCO₂ (top panels) and LE (bottom panels) against tidal range
 339 and latitude, where the points are colored by the size of the dataset. Linear correlations are
 340 shown in bold where slopes are significantly different from zero (b and c; $R^2 = 0.504, < 0.01$
 341 respectively). An estimated mean tidal range at OES of 0.5m (Sahlée et al., 2008) was used for
 342 this figure.

333 3.3. Environmental FCO₂ drivers: Wavelet Coherence

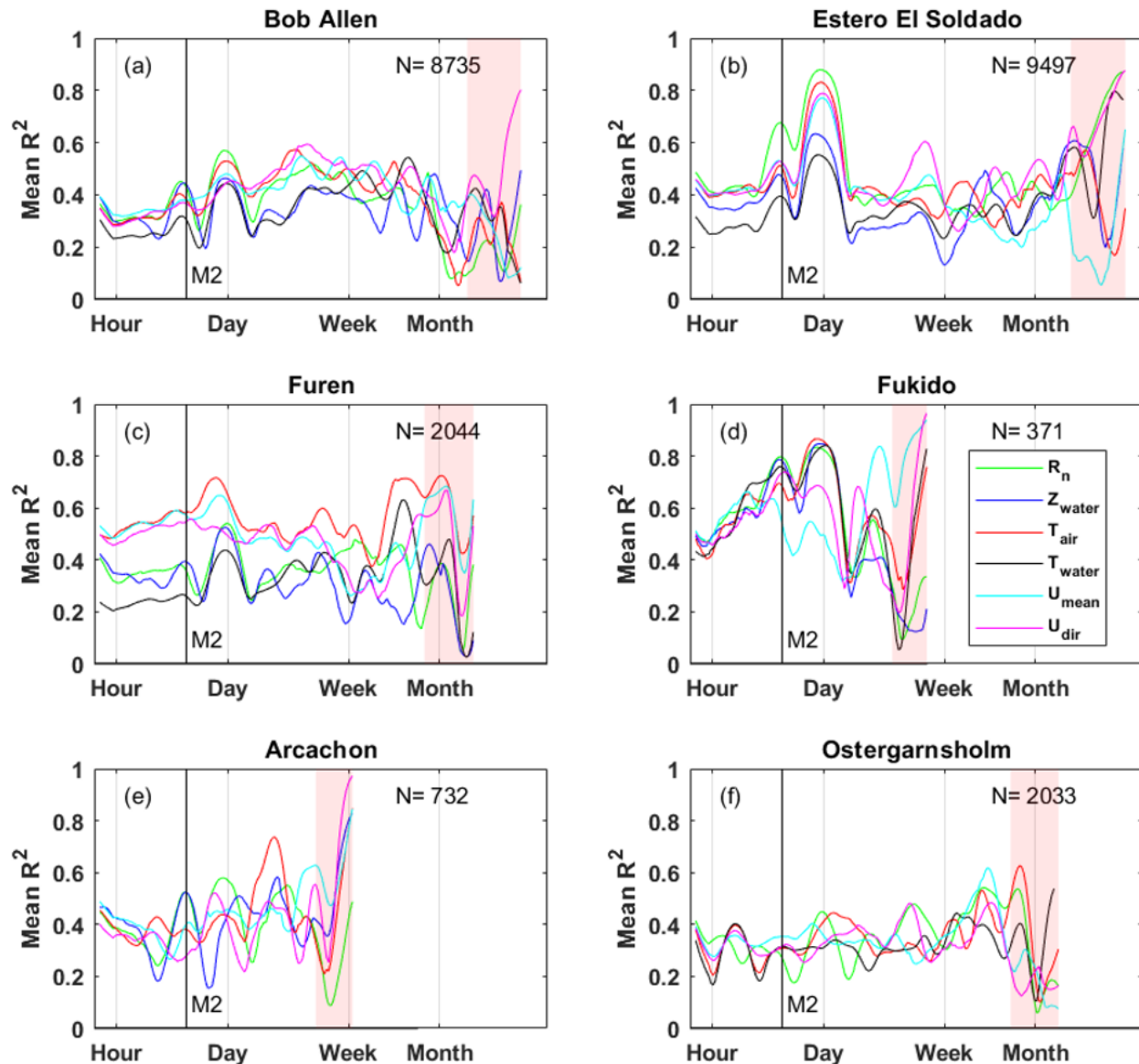
344 Results from the wavelet coherence analysis are shown in Figure S2, for the following selection
 345 of variables: net solar radiation (R_n), water depth (Z_{water}), air temperature (T_{air}), water
 346 temperature (T_{water}), wind speed (U_{mean}), and wind direction (U_{dir}). The color indicates the
 347 strength of the correlation between each variable and FCO₂ with the phase of this relationship
 348 shown by the direction of the arrow. When the variables are in phase (positively correlated), the
 349 arrow points right, out of phase (negative correlation) the arrow points left, and when the driver
 350 leads FCO₂ by 90° the arrow points down. Subsequently, these results are summarized in Figure
 351 7, which presents the average R^2 for the entire period of record, collapsed along the x-axis in Fig
 352 S2. To prevent times of anti-phase correlation from canceling out in-phase correlations (at the
 353 same period), the average presented in Figure 7 was calculated using the absolute value of R^2 . As
 354 such, Figure 7 only represents the average strength, not the direction, of the correlation between
 355 each variable and FCO₂.

356 3.3.1 Weekly-monthly periods

357 The importance of each environmental driver on FCO₂ varied across sites and time scales.
 358 However, at BA and OES there was generally less power at the daily time scale than there was at
 359 weekly-monthly periods. First, as expected for a small-tidal site, Z_{water} was the least predictive

360 variable in the wavelet coherence analysis at BA, even at the semidiurnal lunar tide (M2 period,
361 ~12.5 hrs). This is in line with the results of the energy budget analysis (Figure 2), supporting the
362 concept that tidal forcing was not an important driver of FCO₂ here. Instead, weekly-monthly
363 scale variations in T_{water}, T_{air}, U_{mean}, U_{dir} were especially prominent as drivers of FCO₂, rivaling
364 the impact of diel R_n variability (Figures 7a, S2). In particular, the strong positive correlation
365 between T_{water} and FCO₂ across multiple time scales supports 1) the role of ecosystem
366 calcification as a putative CO₂ source, and 2) the importance of thermal forcing of air-water gas
367 transfer (Van Dam et al., in review).

368 As was the case for BA, power at the M2 period was not elevated at OES, indicating that tidal
369 forcing was not an important driver of FCO₂ here. Instead, power was focused at longer weekly-
370 monthly time scales at OES (and BA). Because much of the variability at these longer periods is
371 due to synoptic- or meso-scale events, it seems likely that weather patterns at these intermediate
372 time scales may be important drivers of FCO₂ at both OES and BA. Such weather events have
373 also been shown to enhance methane emissions at OES (Gutiérrez-Loza et al., 2019). Fluxes at
374 OES are also known to exhibit a strong seasonal cycle (Rutgersson et al., 2020), although the
375 presence of data gaps prevented the incorporation of seasonality into this wavelet coherence
376 analysis. The relatively deep water at this site - from less than 5 to greater than 20 m depending
377 on flux footprint – may also support the dominance of long time-scales at OES.



378
 379 **Figure 7.** Wavelet coherence analysis summary showing the mean power (R^2) for the
 380 relationship between FCO_2 and net solar radiation (R_n), water depth (Z_{water}), air temperature
 381 (T_{air}), water temperature (T_{water}), wind speed (U_{mean}), and wind direction (U_{dir}), averaged over the
 382 length of each dataset (x-axis in Figure S2). The red shading indicates periods where we suspect
 383 uncertainty due to edge effects, estimated as 90% of the maximum period. Because positive and
 384 negative R^2 values cancel out when averaged, we calculated this statistic using absolute value R^2 .
 385 This action effectively sacrifices knowledge of the correlation phase in exchange for a more
 386 intuitive summary of the correlation power.

387 3.3.2 Daily and M2 periods

388 At both EES and FU, there are clear bands of power at the daily and M2 time scales (Figure S2),
 389 supporting the diel trends present in the FCO_2 climatology (Figure 5). At EES, all variables
 390 considered are correlated with FCO_2 at the daily time scale, but these variables trade off in

391 importance over the period of record (Figure S2). For example, U_{mean} is strongly out of phase
392 with FCO_2 during the first half of the study period at EES, while Z_{water} and T_{water} are only weakly
393 correlated with FCO_2 . During the second half of the period of record, this trend reverses, with
394 Z_{water} and T_{water} exceeding U_{mean} as drivers of diel variability in FCO_2 . Seasonal changes in
395 seagrass productivity at EES is a candidate explanation for these longer-term trends in the drivers
396 of diel-scale variability in FCO_2 and is discussed in detail elsewhere. However, we cannot rule
397 out the importance of seasonal upwelling in the eastern Gulf of California (Lluch-Cota 2000),
398 which may introduce cooler, high- pCO_2 coastal waters to the EES system.

399 At FU, the diel trend in FCO_2 was opposite of the trend elsewhere, such that CO_2 uptake was
400 greater at night, and decreased during the day (Figure 5). This may appear counterintuitive, given
401 the expectation of greater CO_2 uptake during the day, as supported by photosynthesis-irradiance
402 curves at this site during the summer (Tokoro et al., 2014). However, these estimates of net
403 ecosystem productivity varied from positive to negative over all light regimes in both summer
404 and winter months (Tokoro et al., 2014), indicating that inorganic carbon fluxes were affected by
405 factors other than net ecosystem primary productivity during this time period. Across all periods,
406 T_{air} was the strongest predictor of FCO_2 at the boreal FU site (Figure S2), such that covariations
407 in T_{air} and FCO_2 are in phase (Figure 7c). This in-phase correlation between FCO_2 and T_{air} (and
408 T_{water}), at FU suggests the thermal impact of changing water temperature on pCO_2 , where pCO_2
409 rises during the day as water warms and decreases over night as solubility increases (Takahashi
410 et al., 2002), in line with prior findings at Bob Allen Keys, Florida (Van Dam et al., in review).
411 As with the other large-tidal sites, correlations between Z_{water} and FCO_2 at FU are strongest at the
412 diel and M2 periods, further supporting the role of tidal forcing on air-water CO_2 exchange.

413 3.3.3 Wavelet coherence: Sites with limited data

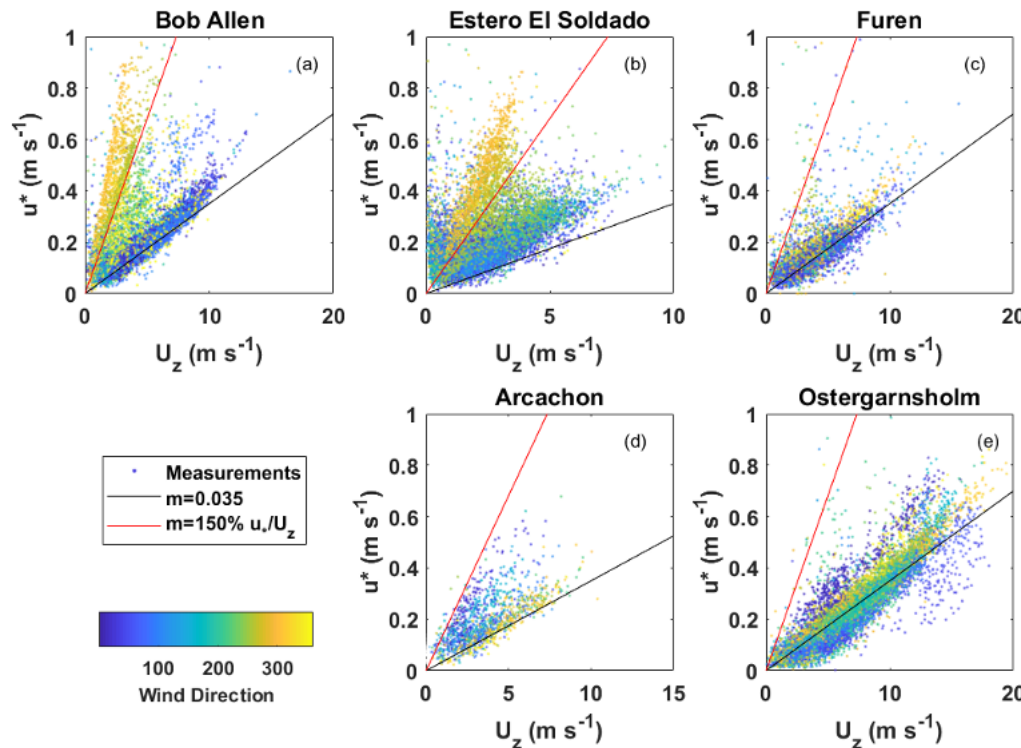
414 Due to the limited length of data for both FK and AR, it was not possible to assess variability at
415 time scales of a week or more. Nevertheless, tidal forcing appeared to play a prominent role at
416 AR, where Z_{water} and FCO_2 were correlated (generally in-phase) at the diel and M2 periods
417 (Figure S2). This is in line with previous findings demonstrating a general trend of CO_2 uptake
418 during low tide and release during high tide at AR (Polsenaere et al., 2012).

419 At FK, strong anti-phase correlations exist at the diel time scale for R_n , T_{water} and T_{air} , while an
420 in-phase relationship is present between FCO_2 and Z_{water} (Figure S2). The presence of anti-phase
421 relationships between FCO_2 and R_n , T_{water} and T_{air} , strongly suggest photosynthetic CO_2 uptake
422 as a driver of FCO_2 during the short period for which measurements are available at FK. Since
423 CO_2 solubility decreases with increasing temperature, one would expect FCO_2 and air or water
424 temperature to be in phase. The existing anti-phase relationship between these variables suggests
425 that something other than thermal forcing, namely biological CO_2 fixation, caused the daytime
426 CO_2 uptake at FK. The combination of shallow water depths (< 2m) and relatively low
427 phytoplankton Chlorophyll-a (Tokoro et al., 2014) suggests that submerged aquatic vegetation,
428 mostly seagrass, were responsible for the majority of this CO_2 uptake. As with the remaining
429 large-tidal sites, the strong power at the M2 period for most variables (Figure 7d), supports tidal
430 forcing as a key driver of FCO_2 .

431 **3.4. Air-side physical drivers of FCO₂**

432 Numerous factors contribute to the physical forcing of gas transfer in shallow coastal waters,
433 including friction with the bottom (Rosentreter et al., 2017; Zappa et al., 2003), water-side
434 convection (Van Dam et al., 2019b, Podgrajsek et al., 2015), breaking waves, biogenic
435 surfactants. Nevertheless, wind speed remains the most commonly-used driver in gas transfer
436 parameterization, even in coastal waters. While a rigorous quantification of gas transfer rates is
437 beyond the scope of this study, our dataset contains valuable information on the turbulent
438 processes responsible for air-sea gas exchange and may help to illustrate features that are
439 globally consistent or variable. Such a comparison is currently absent from the coastal gas-
440 transfer literature.

441 In the open ocean, the transfer of momentum (and therefore gas) between the sea and air is
442 strongly associated with the wind stress (τ), which is proportional to the atmospheric friction
443 velocity (u_*) through τu^2 (Upstill-Goddard 2006). The shape of the relationship between wind
444 speed and u_* , therefore, is of great interest. When sites are mostly surrounded by water, such that
445 the flux footprint is aquatic across most wind directions (FU, OES), u_* increases linearly with
446 wind speed (U_z), at a slope of approximately 0.035 (Figure 8 c,e). At the remaining sites, which
447 experience a terrestrial influence at certain wind directions (BA, EES, AR), there is a clear
448 dependence of the slope on wind direction (Figure 8 a,b,d). At these sites, when the wind
449 direction is such that the flux footprint is entirely aquatic (blue points for Figure 8 a,b), u_* scales
450 with wind speed at the same 0.035 slope. However, when a terrestrial influence is likely (e.g.
451 winds between 180 to 360° at BA), the slope between u_* and wind speed increases and becomes
452 variable, as expected for relatively rough terrestrial surfaces. Since a terrestrial influence is not
453 desirable for the present study, we calculated an average ratio of u_*/U_z (0.0924), and discarded
454 FCO₂ values when this ratio was greater than 150% of the mean (i.e. $u_*/U_z > 0.139$). The
455 associated threshold slope of u_*/U_z is shown as the red line in Figure 8.



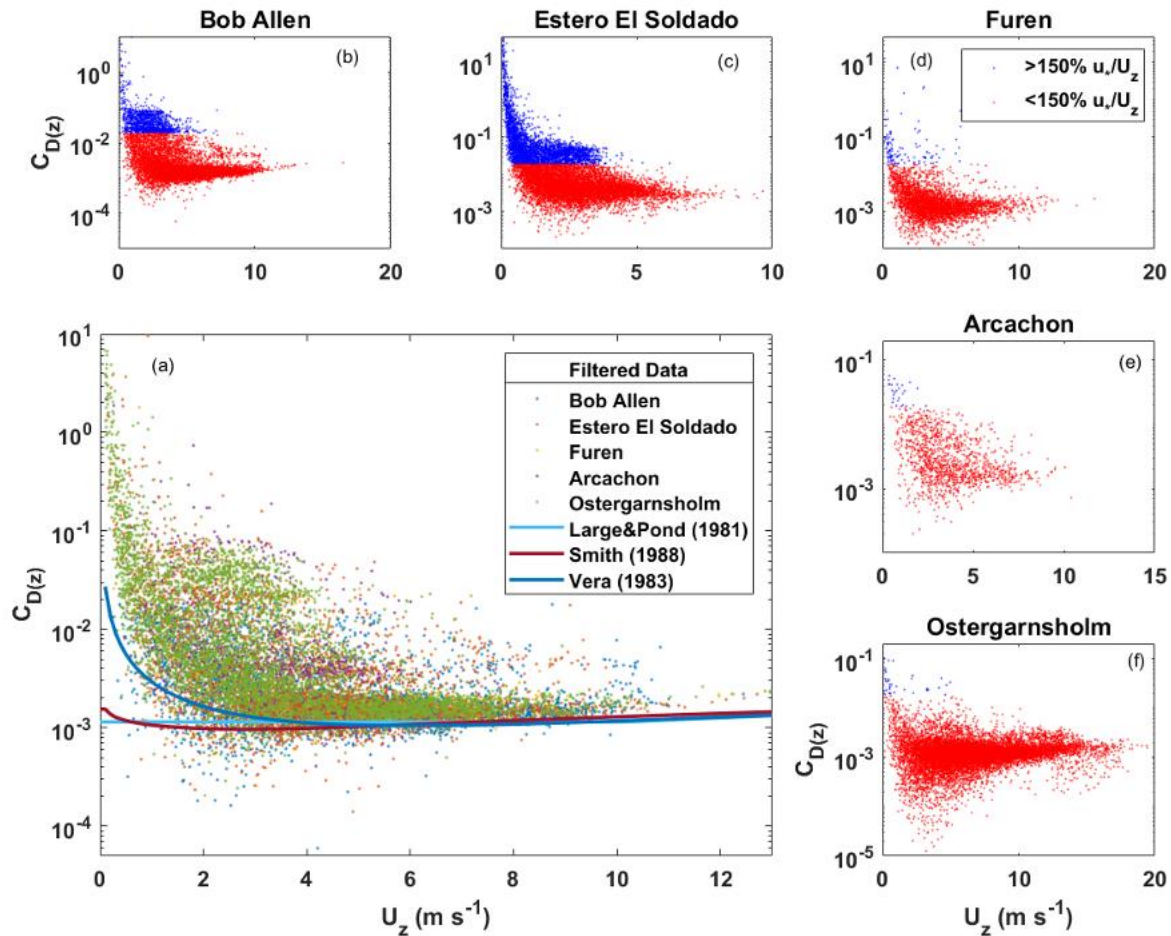
456
 457 **Figure 8.** Wind speed at measurement height (U_z) versus friction velocity across sites, colored
 458 by wind direction. The black line is a reference slope of 0.035, and the red line shows the slope
 459 relating to a u^*/U_z ratio 150% of the average value

460 The nature of momentum transfer (and thereby gas transfer) can be further assessed through the
 461 drag coefficient associated with the measurement height z ($C_{D(z)}$), which is related to the
 462 aforementioned ratio of u^*/U_z through $C_{D(z)} = \frac{u^*}{U_z}$, where U_z is the wind speed (m s^{-1}) at the
 463 measured height. At all sites, calculated values of $C_{D(z)}$ were highly variable with wind speed, but
 464 generally exceed parameterizations for the open ocean by a factor of at least 5-10 (Figure 9a).
 465 The general distribution of $C_{D(z)}$ with U_z fits the pattern observed in Vickers et al. (2013), who
 466 describe three main domains, where 1) $C_{D(z)}$ is large, and not strongly related to U_z ($1-4 \text{ m s}^{-1}$), 2)
 467 moderate winds ($4-10 \text{ m s}^{-1}$) where $C_{D(z)}$ is constant at ~ 0.01 , and 3) a regime of increasing $C_{D(z)}$
 468 at U_z greater than 10 m s^{-1} (only visible for BA and OES in Figure 9b,f).

469 The elevation in $C_{D(z)}$ above values expected for the open ocean may be related to the increased
 470 roughness of immature, ‘growing’ waves under fetch-limited conditions (Mahrt et al., 1996;
 471 Vickers and Mahrt 1997; Rutgersson et al. 2020). Small-scale non-stationary winds have been
 472 shown to enhance fluxes above the theoretical expectations for lower wind speeds in marine
 473 conditions (Mahrt et al., 2020). This $C_{D(z)}$ enhancement may be related to ‘disturbed’ or
 474 ‘growing’ wave fields which may be present at low, as well as high, wind speeds (Rutgersson et
 475 al., 2020). These ‘growing’ wave fields, under non-stationary conditions may offer a possible
 476 explanation for the observed increase in $C_{D(z)}$ at wind speeds between $1-5 \text{ m s}^{-1}$ (Figure 9a).

477 However, it is clear that other factors may also contribute to this $C_{D(z)}$ enhancement, including
 478 bottom-driven turbulence, surfactant activity, shallow water depth (more rapid wave breaking)

479 and the presence of additional submerged roughness elements (i.e. seagrasses). For example, at
 480 very low wind speeds, the combination of increased air-side convection and unstable-to-neutral
 481 conditions has been associated with enhanced gas transfer rates (Sahlee et al., 2008; Van Dam et
 482 al., in review). However, this effect is not clear in the present dataset, as atmospheric stability
 483 (z/L) was not related to these periods of increased $C_{D(z)}$ (not shown).



484 **Figure 9.** Relationship between U_z and $C_{D(z)}$, after filtering by the u^*/U_z threshold (a). A selection
 485 of open-ocean relationships from the literature is depicted in the solid lines. Similar scatterplots
 486 for individual sites, showing all data (b-f), including measurements where u^*/U_z exceeded the
 487 150% threshold which are represented by the blue points.
 488

489 3.5. Global trends

490 While LE fluxes exhibited a significant latitudinal trend, with net evaporative heat losses
 491 increasing towards the equator (Figure 6d), such a trend was not apparent for FCO₂ (Figure 5b).
 492 Instead, tidal forcing appears to be a global driver of FCO₂ trends in seagrass meadows, with
 493 large-tidal sites exhibiting a greater FCO₂ range (Figure 4), and magnitude toward a CO₂ sink
 494 status (Figure 6b), than small-tidal sites. Furthermore, small-tidal sites (BA, OES) responded
 495 strongly to variability at time scales longer than a day (Section 3.3.1), while the large-tidal sites
 496 (EES, FU, FK) were more sensitive to variability at the M2 and daily time scales (Section 3.3.2).

497 Many factors may contribute to this global trend in tidal forcing of air-water CO₂ exchange.
498 Tidal currents can enhance rates of gas transfer when bottom-generated turbulence impacts the
499 air-water interface (Ho et al., 2014; Rosentreter et al., 2017; Upstill-Goddard 2006), but under
500 certain conditions may suppress gas transfer when currents are strong enough to re-suspend
501 sediments (Abril et al., 2009). Similarly, tidal impacts on sediment biogeochemical cycling can
502 cause variations in the air-water CO₂ gradient. Sediment resuspension and tidal oxygen pumping
503 can enhance rates of aerobic respiration enhancing CO₂ release (Almroth-Rosell, et al., 2012;
504 Ståhlberg et al., 2006). Elsewhere, current can generate pressure gradients which flush anaerobic
505 respiration products from sediments, either increasing or decreasing pCO₂ in proportion to DIC
506 and alkalinity fluxes (Santos et al., 2015). At a larger scale, tidal mixing drives inorganic carbon
507 “outwelling” from coastal marshes (Cai et al., 1999), with an effect on air-water CO₂ exchange
508 that should be proportional to the DIC:TA export ratio. Because these factors act synchronously,
509 it is impossible to attribute the global trend of decreasing magnitude and range in FCO₂ with a
510 single ‘tidal’ factor. Nevertheless, it is clear that tidal dynamics must be considered when the net
511 carbon sink/source status of seagrass meadows is assessed.

512 **4. Summary and conclusion**

513 We produced a global synthesis of all available eddy covariance measurements of air-water CO₂
514 exchange (FCO₂) over shallow, seagrass-dominated environments. At most sites, the absolute
515 magnitude of FCO₂ was as large or larger than published “blue carbon” burial rates (CBR).
516 Elsewhere, CO₂ fluxes in excess of organic carbon storage have been reported for Japanese
517 seagrasses (Kuwae and Hori 2019), but the present study demonstrates that this is a global, not
518 regional phenomenon. At seagrass meadows functioning as net sources of CO₂ to the atmosphere
519 (BA, OES), FCO₂ was between 44 (OES) -115 (BA)% of global average CBR (0.13 μmol m⁻² s⁻¹
520 ¹). Assuming minimal lateral exchange, this effectively converted BA from a net carbon sink into
521 a net carbon source. Datasets for both BA and OES contain substantial and representative
522 measurements during all seasons (Figure 5b), indicating that while there is substantial seasonal
523 variability (Rutgersson et al., 2020) in FCO₂, these sites are indeed both net sources of CO₂ to
524 the atmosphere. We suggest net ecosystem calcification as a putative source of this CO₂, due to
525 the correlation between FCO₂ and temperature, and the large CaCO₃ stocks present at this site
526 (Howard et al., 2018). For the remaining sites, net CO₂ uptake was ~100% (EES) to over 800%
527 (FU) of global average CBR. However, additional seasonal measurements would improve the
528 reliability of this assessment.

529 We then identified drivers of FCO₂ that are present across the large range in seagrass
530 ecosystems, which are responsible for generating this ‘disagreement’ between CBR and net
531 carbon sink/source status. First, we considered the leverage exerted on FCO₂ by the physical
532 processes affecting rates of air-water CO₂ exchange, and found that surface roughness (C_{D(z)})
533 was always greater than expected for the open ocean, suggesting a near-universal enhancement
534 of gas transfer in shallow, coastal waters. Next, many lines of evidence point to tidal-driven
535 exchanges as a key driver for FCO₂ over seagrass meadows. First, we show a clear relationship
536 between tidal range and energy balance residual, which persists across our global range in study
537 sites. This energy balance ‘leakage’ under tidal conditions indicates that the lateral exchange of

538 dissolved CO₂ (and organic carbon) is a major factor contributing to the observed mismatch
539 between FCO₂ and CBR. The negative relationship between average tidal range and FCO₂
540 (Figure 6) provides further evidence that the sites acting as net CO₂ sinks may have done so in
541 response to tidal forcing. Lastly, the results of our wavelet coherence analysis support the role of
542 tidal forcing on FCO₂, given the increase in power at the M2 period, especially for EES, AR, and
543 FU (Figure 9b,c,e).

544 In conclusion, we report high rates of air-water CO₂ exchange over seagrass meadows, which
545 may significantly alter the net carbon storage capacity of these ‘blue carbon’ ecosystems. This
546 study argues the need for a more comprehensive approach to future ‘blue carbon’ assessments,
547 which should consider organic carbon storage in the context of other carbon fluxes, including
548 air-water CO₂ exchange. Future studies can build on this work by investigating the role of tidal
549 and thermal forcing, which may affect CO₂ fluxes by enhancing (or suppressing) the turbulence
550 responsible for air-water gas exchange, but may also transport excess CO₂ away from or to
551 seagrass meadows. And, while the present study was limited to CO₂, many of the factors
552 affecting air-sea CO₂ transfer are also apply to other greenhouse gases including CH₄ and N₂O.
553 There is also a clear need for direct CO₂ flux measurements in the southern hemisphere, of which
554 none are presently available.

555 **Acknowledgments**

556 This work was primarily supported by the DAAD grant #57429828, from funds of the German Federal
557 Ministry of Education and Research (BMBF). This work was supported by the US National Science
558 Foundation through the Florida Coastal Everglades Long-Term Ecological Research program under
559 Grants No. DEB-1237517 and DEB-1832229. We thank Prof Dr Helmuth Thomas and Dr Mary Zeller
560 for their feedback on this manuscript, which significantly improved its quality. Technical staff at LI-COR
561 were also indispensable, and we specifically thank Israel Begashaw and James Kathilankal for their
562 patience and support. We also appreciate the assistance of the National Parks Service, who allowed
563 equipment to be deployed in the Everglades National Park at Bob Allen Keys, under Permit [EVER-2018-
564 SCI-0072]. Measurements at Estero El Soldado were possible with funds from the Mexican National
565 Council of Science and Technology (CONACYT) grant # 278608 and assistance of the Ecology
566 Commission from Sonora (CEDES). This is contribution #[updated upon publication] from the Coastlines
567 and Oceans Division in The Institute of Environment at Florida International University. TK and TT was
568 funded in part by Grants-in-Aid for Scientific Research (KAKENHI) grant numbers JP18H04156 from
569 the Japan Society for the Promotion of Science. The Östergarnsholm site is a part of the ICOS (Integrated
570 Carbon Observation Study) and funded by Swedish Research Council and Uppsala University. Technical
571 staff working at the Östergarnsholm station are greatly acknowledged. The Arcachon study was supported
572 by the ANR project PROTIDAL and the Aquitaine region; we are grateful to all our colleagues from the
573 University of Bordeaux and INRA Bordeaux who participated to EC field deployments, data analysis and
574 associated constructive reflexions.

575 Data Availability Statement

576 Data are published openly at doi 10.6084/m9.figshare.12161478 for BA, and 10.5281/zenodo.3372787
577 for EES. The remaining datasets for FU, FK, AR, and OES are available under previous publications
578 Tokoro et al. (2014), Polsenaere et al. (2012), and Rutgersson et al. (2020).

579 Competing Interests

580 The authors declare no conflicts of interest

581 References

- 582 Abril, G., Commarieu, M. V., Sottolichio, A., Bretel, P., & Guérin, F. (2009). Turbidity limits
583 gas exchange in a large macrotidal estuary. *Estuarine, Coastal and Shelf Science*, 83(3),
584 342–348. <https://doi.org/10.1016/j.ecss.2009.03.006>
- 585 Almroth-Rosell, E., Tengberg, A., Andersson, S., Apler, A., & Hall, P. O. J. J. (2012). Effects of
586 simulated natural and massive resuspension on benthic oxygen, nutrient and dissolved
587 inorganic carbon fluxes in Loch Creran, Scotland. *Journal of Sea Research*, 72, 38–48.
588 <https://doi.org/10.1016/j.seares.2012.04.012>
- 589 Al-Haj, A. N., & Fulweiler, R. W. (2020). A synthesis of methane emissions from shallow
590 vegetated coastal ecosystems. *Global Change Biology*, 26(5), 2988–3005.
591 <https://doi.org/10.1111/gcb.15046>
- 592 Armitage, A. R., Frankovich, T. A., & Fourqurean, J. W. (2011). Long-Term Effects of Adding
593 Nutrients to an Oligotrophic Coastal Environment. *Ecosystems*, 14(3), 430–444.
594 <https://doi.org/10.1007/s10021-011-9421-2>
- 595 Aubinet, M., Grelle, A., Ibrom, A., Rannik, U., Moncrieff, J., Foken, T., Kowalski, A. S., Martin,
596 P. H., Berbigier, P., Bernhofer, C. H., Clement, R., Elbers, J., Granier, A., Grunwald, T.,
597 Morgenstern, K., Pilegaard, K., Rebmann, C., Snijders, W., Valentini, R., and Vesala, T.:
598 Estimates of the annual net carbon and water exchange of European forests: the
599 EUROFLUX methodology, *Adv. Ecol. Res.*, 30, 113–175, 2000.
- 600 Barreras-Apodaca, A. & Sánchez-Mejía, Z.M. (2019). Eddy Covariance observations of three
601 different sites from Estero El Soldado, Sonora, Mexico, doi:10.5281/zenodo.3372787
- 602 Benítez-Valenzuela, L. I., & Sanchez-Mejia, Z. M. (2020). Observations of turbulent heat fluxes
603 variability in a semiarid coastal lagoon (Gulf Of California). *Atmosphere*, 11(6), 15–17.
604 <https://doi.org/10.3390/atmos11060626>
- 605 Berg, P., Delgard, M. L., Polsenaere, P., Mcglathery, K. J., Doney, S. C., & Berger, A. C.
606 (2019). Dynamics of benthic metabolism, O₂, and pCO₂ in a temperate seagrass meadow.
607 *Limnology and Oceanography*, 1–19. <https://doi.org/10.1002/lno.11236>.
- 608 Burba, G. (2010). *Eddy Covariance Method for Scientific, Industrial, Agricultural, and*
609 *Regulatory Applications*. LI-COR Biosciences, Lincoln, Nebraska. ISBN: 978-0-615-76827-4

- 610 Burdige, D. J., & Zimmerman, R. C. (2002). Impact of Sea Grass Density on Carbonate
611 Dissolution in Bahamian Sediments Impact of sea grass density on carbonate dissolution in
612 Bahamian sediments. *Limnology and Oceanography*, 47, 1751–1763.
613 <https://doi.org/10.4319/lo.2002.47.6.1751>
- 614 Burdige, D. J., Hu, X., & Zimmerman, R. C. (2010). The widespread occurrence of coupled
615 carbonate dissolution/precipitation in surface sediments on the Bahamas Bank. *American*
616 *Journal of Science*, 310(6), 492–521. <https://doi.org/10.2475/06.2010.03>
- 617 Carmen B, Krause-Jensen D, Alcoverro T, Marbà N, Duarte CM, van Katwijk MM, Pérez M,
618 Romero J, Sánchez-Lizaso JL, Roca G, Jankowska E, Pérez-Lloréns JL, Fournier J,
619 Montefalcone M, Pergent G, Ruiz JM, Cabaço S, Cook K, Wilkes RJ, Moy FE, Trayter
620 GMR, Arañó XS, de Jong DJ, Fernández-Torquemada Y, Auby I, Vergara JJ, Santos R.
621 2019. Recent trend reversal for declining European seagrass meadows. *Nature*
622 *Communications* 10:3356.
- 623 Cai, W.-J., Pomeroy, L. R., Moran, M. A., & Wang, Y. (1999). Oxygen and carbon dioxide mass
624 balance for the estuarine-intertidal marsh complex of five rivers in the Southeastern U.S.
625 *Limnology and Oceanography*, 44(3), 639–649. <https://doi.org/10.4319/lo.1999.44.3.0639>
- 626 Dürr, H. H., Laruelle, G. G., van Kempen, C. M., Slomp, C. P., Meybeck, M., & Middelkoop, H. (2011).
627 Worldwide typology of nearshore coastal systems: Defining the estuarine filter of river inputs to the
628 oceans. *Estuaries and Coasts*, 34(3), 441–458. <https://doi.org/10.1007/s12237-011-9381-y>
- 629 Dollar, S. J., Smith, S. V., Vink, S. M., Obrebski, S., & Hollibaugh, J. T. (1991). Annual cycle of
630 benthic nutrient fluxes in Tomales Bay, California, and contribution of the benthos to total
631 ecosystem metabolism. *Marine Ecology Progress Series*, 79(1–2), 115–125.
632 <https://doi.org/10.3354/meps079115>
- 633 Duarte, C. M., Middelburg, J. J., & Caraco, N. (2005). Major role of marine vegetation on the
634 oceanic carbon cycle. *Biogeosciences*, 2, 1–8. <https://doi.org/10.5194/bg-2-1-2005>
- 635 Duarte, C. M., Marbà, N., Gacia, E., Fourqurean, J. W., Beggins, J., Barrón, C., & Apostolaki, E.
636 T. (2010). Seagrass community metabolism: Assessing the carbon sink capacity of seagrass
637 meadows. *Global Biogeochemical Cycles*, 24(4), 1–8.
638 <https://doi.org/10.1029/2010GB003793>
- 639 Eyre, B. D., & Ferguson, A. J. P. (2002). Comparison of carbon production and decomposition,
640 benthic nutrient fluxes and denitrification in seagrass, phytoplankton, benthic microalgae-
641 and macroalgae-dominated warm-temperate Australian lagoons. *Marine Ecology Progress*
642 *Series*, 229, 43–59. <https://doi.org/10.3354/meps229043>
- 643 Fennel, K., Alin, S., Wang, Z. A., Barbero, L., Shadwick, E., Cooley, S., ... Hernandez-Ayon, J.
644 M. (2019). Carbon cycling in the North American coastal ocean: A synthesis.
645 *Biogeosciences Discussions*, 16, 1281–1304. <https://doi.org/10.5194/bg-2018-420>

- 646 Fourqurean, J. W., Duarte, C. M., Kennedy, H., Marbà, N., Holmer, M., Mateo, M. A., ...
647 Serrano, O. (2012). Seagrass ecosystems as a globally significant carbon stock. *Nature*
648 *Geoscience*, 5(7), 505–509. <https://doi.org/10.1038/ngeo1477>
- 649 Friedlingstein, P., Jones, M. W., O’Sullivan, M., Andrew, R. M., Hauck, J., Peters, G. P., ...
650 Zaehle, S. (2019). Global carbon budget 2019. *Earth System Science Data*, 11(4), 1783–
651 1838. <https://doi.org/10.5194/essd-11-1783-2019>
- 652 Gazeau, F., Borges, A. V., Barrón, C., Duarte, C. M., Iversen, N., Middelburg, J. J., ... Gattuso,
653 J. P. (2005). Net ecosystem metabolism in a micro-tidal estuary (Randers Fjord, Denmark):
654 Evaluation of methods. *Marine Ecology Progress Series*, 301, 23–41.
655 <https://doi.org/10.3354/meps301023>
- 656 Grinsted, A., Moore, J.C., Jevrejeva, S., 2004. Application of the cross wavelet transform and
657 wavelet coherence to geophysical time series. *Nonlinear processes in geophysics* 11, 561-
658 566.
- 659 Gutiérrez-Loza, L., Wallin, M. B., Sahlée, E., Nilsson, E., Bange, H. W., Kock, A., & Rutgersson, A.
660 (2020). Measurement of Air-Sea Methane Fluxes in the Baltic Sea Using the Eddy Covariance
661 Method. *Frontiers in Earth Science*, 7(May), 1–13. <https://doi.org/10.3389/feart.2019.00093>
- 662 Ho, D. T., Ferrón, S., Engel, V. C., Larsen, L. G., & Barr, J. G. (2014). Air-water gas exchange
663 and CO₂ flux in a mangrove-dominated estuary. *Geophysical Research Letters*, 41(1),
664 108–113. <https://doi.org/10.1002/2013GL058785>
- 665 Howard, J. L., Creed, J. C., Aguiar, M. V. P., & Fouqurean, J. W. (2018). CO₂ released by carbonate
666 sediment production in some coastal areas may offset the benefits of seagrass “Blue Carbon”
667 storage. *Limnology and Oceanography*, 63(1), 160–172. <https://doi.org/10.1002/lno.10621>
- 668 Hu, X., & Burdige, D. J. (2007). Enriched stable carbon isotopes in the pore waters of carbonate
669 sediments dominated by seagrasses: Evidence for coupled carbonate dissolution and
670 reprecipitation. *Geochimica et Cosmochimica Acta*, 71(1), 129–144.
671 <https://doi.org/10.1016/j.gca.2006.08.043>
- 672 Kennedy, H., Beggins, J., Duarte, C. M., Fourqurean, J. W., Holmer, M., Marbà, N., & Middelburg, J. J.
673 (2010). Seagrass sediments as a global carbon sink: Isotopic constraints. *Global Biogeochemical*
674 *Cycles*, 24(4), 1–8. <https://doi.org/10.1029/2010GB003848>
- 675 Kuwae, T., & Hori, M. (2019). Blue Carbon in Shallow Coastal Ecosystems. In *Blue Carbon in*
676 *Shallow Coastal Ecosystems*. <https://doi.org/10.1007/978-981-13-1295-3>
- 677 Laruelle, G. G., Cai, W. J., Hu, X., Gruber, N., Mackenzie, F. T., & Regnier, P. (2018).
678 Continental shelves as a variable but increasing global sink for atmospheric carbon dioxide.
679 *Nature Communications*, 9(1), 1–11. <https://doi.org/10.1038/s41467-017-02738-z>
- 680 Legge, O., Martin Johnson, Natalie Hicks, Tim Jickells, Markus Diesing, John Aldridge, J.,
681 Andrews, Yuri Artioli, Dorothee C. E. Bakker, Michael T. Burrows, Nealy Carr, G. C.,

- 682 Stacey Felgate , Liam Fernand , Naomi Greenwood , Sue Hartman , Silke Kröger, G. L.,
683 Claire Mahaffey , Daniel J Mayor , Ruth Parker , Ana M Queirós , Jamie D. Shutler, T. S.,
684 Henrik Stahl , Jonathan Tinker , Graham J.C. Underwood , Johan van der Molen, S. W., &
685 Keith Weston, P. W. (2020). Carbon on the Northwest European Shelf: Contemporary
686 Budget and Future Influences. *Frontiers in Marine Science Specialty*, 7(March).
687 <https://doi.org/10.3389/fmars.2020.00143>
- 688 Long, M., Berg, P., & Falter, J. (2015). Seagrass metabolism across a productivity gradient using
689 the eddy covariance, Eulerian control volume, and biomass addition techniques. *Journal of*
690 *Geophysical Research: Oceans*, 120, 2676–2700. <https://doi.org/10.1002/2014JC010441>
- 691 Long, M., Berg, P., & Falter, J. (2015). Seagrass metabolism across a productivity gradient using
692 the eddy covariance, Eulerian control volume, and biomass addition techniques. *Journal of*
693 *Geophysical Research: Oceans*, 120, 2676–2700. <https://doi.org/10.1002/2014JC010441>
- 694 Lluch-Cota, S.-E. (2000). Coastal upwelling in the eastern Gulf of California. *Oceanologica*
695 *Acta*, 23, 731–740.
- 696 Macreadie, P. I., Serrano, O., Maher, D. T., Duarte, C. M., & Beardall, J. (2017). Addressing
697 calcium carbonate cycling in blue carbon accounting. *Limnology and Oceanography*
698 *Letters*, (Tyrrell 2008), 195–201. <https://doi.org/10.1002/lol2.10052>
- 699 Macreadie, P. I., Et. al. (2019). The future of Blue Carbon science. *Nature Communications*, 1–
700 13. <https://doi.org/10.1038/s41467-019-11693-w>
- 701 Mahrt, L., Vickers, D., Howell, J., Højstrup, J., Wilczak, J. M., Edson, J., & Hare, J. (1996). Sea
702 surface drag coefficients in the Risø Air Sea Experiment. *Journal of Geophysical Research*
703 *C: Oceans*, 101(C6), 14327–14335. <https://doi.org/10.1029/96JC00748>
- 704 Mahrt, L., E. Nilsson, H. Pettersson and A. Rutgersson (2020) Sea-surface stress driven by
705 small-scale non-stationary winds. *Bound. Layer Met.*, <https://doi.org/10.1007/s10546-020-00518-9>
- 706
- 707 Oreska, M. P. J., McGlathery, K. J., Aoki, L. R., Berger, A. C., Berg, P., & Mullins, L. (2020). The
708 greenhouse gas offset potential from seagrass restoration. *Scientific Reports*, 10(1), 1–15.
709 <https://doi.org/10.1038/s41598-020-64094-1>
- 710 Perez, D. I., Phinn, S. R., Roelfsema, C. M., Shaw, E., Johnston, L., & Iguel, J. (2018). Primary
711 Production and Calcification Rates of Algae-Dominated Reef Flat and Seagrass Communities.
712 *Journal of Geophysical Research: Biogeosciences*, 123(8), 2362–2375.
713 <https://doi.org/10.1029/2017JG004241>
- 714 Plus M., Dalloyau S., Trut G., Auby I., De Montaudouin X., Emery É., Noël C., Viala C. (2010).
715 Long-term evolution (1988–2008) of *Zostera* spp. meadows in Arcachon Bay (Bay of
716 Biscay). *Estuarine, Coastal and Shelf Science*, 87(2), 357–366.

- 717 Podgrajsek, Sahlée, and Rutgersson (2015), Diel cycle of lake-air CO₂ flux from a shallow lake
 718 and the impact of waterside convection on the transfer velocity, *J. Geophys. Res.*
 719 *Biogeosciences*, doi:10.1002/2014JG002781.
- 720 Polsenaere, P., Lamaud, E., Lafon, V., Loustau, D., Delille, B., Deborde, J., ... Abril, G. (2012).
 721 Spatial and temporal CO₂ exchanges measured by Eddy Covariance over a temperate
 722 intertidal flat and their relationships to net ecosystem production. *Biogeosciences*, 9(1),
 723 249–268. <https://doi.org/10.5194/bg-9-249-2012>
- 724 Prentice, C., Poppe, K. L., Lutz, M., Murray, E., Stephens, T. A., Spooner, A., ... Klinger, T.
 725 (2020). A Synthesis of Blue Carbon Stocks, Sources, and Accumulation Rates in Eelgrass
 726 (*Zostera marina*) Meadows in the Northeast Pacific. *Global Biogeochemical Cycles*, 34(2),
 727 1–16. <https://doi.org/10.1029/2019gb006345>
- 728 Röhr, M. E., Holmer, M., Baum, J. K., Björk, M., Chin, D., Chalifour, L., ... Deyanova, D.
 729 (2018). Blue Carbon Storage Capacity of Temperate Eelgrass (*Zostera marina*) Meadows.
 730 *Global Biochemical Cycles*, 1457–1475. <https://doi.org/10.1029/2018GB005941>
- 731 Rosentreter, J. A., Maher, D. T., Ho, D. T., Call, M., Barr, J. G., & Eyre, B. D. (2017). Spatial
 732 and temporal variability of CO₂ and CH₄ gas transfer velocities and quantification of the
 733 CH₄ microbubble flux in mangrove dominated estuaries. *Limnology and Oceanography*,
 734 62(2), 562–578. <https://doi.org/10.1002/lno.10444>
- 735 Rutgersson, A., Heidi Pettersson, Erik Nilsson, Hans Bergström, Marcus B.E. Wallin, E.
 736 Douglas Nilsson, Erik Sahlée, Lichuan E. Wu & E. Monica Mårtensson (2020) Using land-
 737 based stations for air–sea interaction studies, *Tellus A: Dynamic Meteorology and*
 738 *Oceanography*, 72:1, 1-23, DOI: 10.1080/16000870.2019.1697601
- 739 Saderne, V., Geraldi, N. R., Macreadie, P. I., Maher, D. T., Middelburg, J. J., Serrano, O., ...
 740 Duarte, C. M. (2019). Role of carbonate burial in Blue Carbon budgets. *Nature*
 741 *Communications*, 10. <https://doi.org/10.1038/s41467-019-08842-6>
- 742 Sahlée, E., Smedman, A.-S., Högström, U., & Rutgersson, A. (2008). Reevaluation of the Bulk
 743 Exchange Coefficient for Humidity at Sea during Unstable and Neutral Conditions. *Journal*
 744 *of Physical Oceanography*, 38(1), 257–272. <https://doi.org/10.1175/2007jpo3754.1>
- 745 Samper-Villarreal, J., Mumby, P. J., Saunders, M. I., Barry, L. A., Zawadzki, A., Heijnis,
 746 H., Morelli, G., & Lovelock, C. E. (2018). Vertical accretion and carbon burial rates in
 747 subtropical seagrass meadows increased following anthropogenic pressure from European
 748 colonisation. *Estuarine Coastal and Shelf Science*, **202**, 40– 53.
- 749 Sanders, C. J., Maher, D. T., Smoak, J. M., & Eyre, B. D. (2019). Large variability in organic
 750 carbon and CaCO₃ burial in seagrass meadows: A case study from three Australian
 751 estuaries. *Marine Ecology Progress Series*, 616, 211–218.
 752 <https://doi.org/10.3354/meps12955>

- 753 Santos, I. R., Beck, M., Brumsack, H.-J. J., Maher, D. T., Dittmar, T., Waska, H., & Schnetger,
754 B. (2015). Porewater exchange as a driver of carbon dynamics across a terrestrial-marine
755 transect: Insights from coupled ^{222}Rn and pCO_2 observations in the German Wadden Sea.
756 *Marine Chemistry*, 171, 10–20. <https://doi.org/10.1016/j.marchem.2015.02.005>
- 757 Ståhlberg, C., Bastviken, D., Svensson, B. H., & Rahm, L. (2006). Mineralisation of organic
758 matter in coastal sediments at different frequency and duration of resuspension. *Estuarine,
759 Coastal and Shelf Science*, 70(1–2), 317–325. <https://doi.org/10.1016/j.ecss.2006.06.022>
- 760 Takahashi, T., Sutherland, S. C., Sweeney, C., Poisson, A., Metzl, N., Tilbrook, B., ... Nojiri, Y.
761 (2002). Global sea – air CO_2 flux based on climatological surface ocean pCO_2 , and
762 seasonal biological and temperature effects. *Deep Sea Research Part II: Topical Studies in
763 Oceanography*, 49(9–10), 1601–1622. [https://doi.org/10.1016/S0967-0645\(02\)00003-6](https://doi.org/10.1016/S0967-0645(02)00003-6)
- 764 Tokoro, T., Hosokawa, S., Miyoshi, E., Tada, K., Watanabe, K., Montani, S., ... Kuwae, T. (2014). Net
765 uptake of atmospheric CO_2 by coastal submerged aquatic vegetation. *Global Change Biology*,
766 20(6), 1873–1884. <https://doi.org/10.1111/gcb.12543>
- 767 Tokoro, T., & Kuwae, T. (2018). *Improved Post-processing of Eddy-Covariance Data to
768 Quantify Atmosphere – Aquatic Ecosystem CO_2 Exchanges*. 5(August), 1–11.
769 <https://doi.org/10.3389/fmars.2018.00286>
- 770 Torrence, C., Compo, G.P., 1998. A practical guide to wavelet analysis. *Bulletin of the American
771 Meteorological society* 79, 61-78.
- 772 Upstill-Goddard, R. C. (2006). Air–sea gas exchange in the coastal zone. *Estuarine, Coastal and
773 Shelf Science*, 70(3), 388–404. <https://doi.org/10.1016/j.ecss.2006.05.043>
- 774 Vickers, D., Mahrt, L. (1997). Fetch Limited Drag Coefficients. *Boundary-Layer
775 Meteorology* 85, 53–79. <https://doi.org/10.1023/A:1000472623187>
- 776 Vickers, D., Mahrt, L., & Andreas, E. L. (2013). Estimates of the 10-m Neutral Sea Surface Drag
777 Coefficient from Aircraft Eddy-Covariance Measurements. *Journal of Physical
778 Oceanography*, 43(2), 301–310. <https://doi.org/10.1175/JPO-D-12-0101.1>
- 779 Van Dam, B. R., Lopes, C., Osburn, C. L., & Fourqurean, J. W. (2019a). Net heterotrophy and
780 carbonate dissolution in two subtropical seagrass meadows. *Biogeosciences*, 16, 4411–
781 4428. <https://doi.org/10.5194/bg-2019-191>
- 782 Van Dam, B. R., Edson, J. B., & Tobias, C. (2019b). Parameterizing Air-Water Gas Exchange in
783 the Shallow, Microtidal New River Estuary. *Journal of Geophysical Research:
784 Biogeosciences*, 2018JG004908. <https://doi.org/10.1029/2018JG004908>
- 785 Zappa, C. J., Raymond, P. A., Terray, E. A., & Mcgillis, W. R. (2003). Variation in Surface
786 Turbulence and the Gas Transfer Velocity in a Macro-Tidal Estuary. *Estuaries*, 26(6),
787 1401–1415.